nature communications

Article

https://doi.org/10.1038/s41467-025-58877-1

Edge polarization topology integrated with sliding ferroelectricity in Moiré system

Received: 2 January 2025

Accepted: 4 April 2025

Published online: 15 April 2025

Check for updates

Wen-Cheng Fan[1,5], Zhao Guan[1,5], Lu-Qi Wei[1,5], Hao-Wen Xu[1,5], Wen-Yi Tong[1,2,5], Ming Tian[3], Neng Wan[3], Cheng-Shi Yao[1], Jun-Ding Zheng[1], Bin-Bin Chen[1], Ping-Hua Xiang[1,4] ✉, Ni Zhong[1,4] ✉ & Chun-Gang Duan[1,4] ✉

Van der Waals moiré heterostructure have been found to exhibits a robust interfacial ferroelectricity down to atomic thickness, and discovering and understanding the complex polarization state in moiré systems is of fundamental interest to condensed-matter research. In this study, we examine the moiré ferroelectricity in twisted h-BN heterostructure by piezoresponse force microscopy. Due to atomic reconstruction, triangular moiré patterns are detected, and we directly observe sliding ferroelectricity in the center of triangular moiré patterns as well as robust in-plane polarization topology emerging at the boundary of adjacent triangles, which we call edge polarization. The edge polarization possesses non-trivial and robust vortex polarization topology. Our calculations trace the origin of this phenomenon to joined piezoelectric effects with sliding ferroelectricity. This work provides intuitive insights to explore the unique moiré ferroelectricity in non-polar background matrix, and the inherent stability of the topological structures ensures reliable and durable performance of electronic devices.

Superlattices formed by stacking two-dimensional van der Waals (vdW) materials have garnered significant interest due to their intriguing physics that significantly differs from conventional physics, which possesses potential applications in nanotechnology[1]. By controlling the twist angle, various optical and electronic characteristics, such as superconductivity[2,3], quantum anomalous Hall effect[4], negative capacitance[5], and so on[6–8] can be obtained. Interestingly, if layering sheets slide or twist minor, sliding or moiré ferroelectricity with atomic reconstruction can be obtained[9]. The induced long-range polar structure is generally considered to originate from charge transfer or electron orbital distortion among layers, thereby inducing vertical polar vectors[10]. The nanoscale characterization based on scanning probe microscopy (SPM) is capable of detecting the localized moiré domains, polarization, and charges.

The strong moiré ferroelectricity can emerge in different non-polar systems[11], such as boron nitride (BN)[12–17], WSe_2[16,18–20], and graphene[9,21,22], etc. These ultrathin two-dimensional layered materials lack dangling bonds and can be easily exfoliated to a monolayer. The layered structure ensures unique electronic properties, and their ferroelectricity can persist at atomic-level thickness, thereby overcoming traditional size effects in ferroelectric materials and providing pathways for next-generation storage device applications. However, the physical origins of the moiré systems are much more complicated. More than sliding ferroelectricity, other mechanisms including flexoelectricity[23,24], piezoelectricity[25], are also put forward to explain the unique stacking-induced ferroic properties. Recently, several nontrivial ferroelectric topological configurations such as skyrmions, merons, and vortices[26] have been theoretically demonstrated in twisted low-dimensional vdW heterostructure[27,28]. The long-period moiré

[1]Key Laboratory of Polar Materials and Devices, Ministry of Education & Shanghai Center of Brain-inspired Intelligent Materials and Devices, East China Normal University, Shanghai, China. [2]Suzhou Laboratory, Suzhou, People's Republic of China. [3]Key Laboratory of MEMS of Ministry of Education, School of Integrated Circuits, Southeast University, Nanjing, China. [4]Collaborative Innovation Center of Extreme Optics, Shanxi University, Taiyuan, Shanxi, China. [5]These authors contributed equally: Wen-Cheng Fan, Zhao Guan, Lu-Qi Wei, Hao-Wen Xu, Wen-Yi Tong. ✉e-mail: phxiang@ee.ecnu.edu.cn; nzhong@ee.ecnu.edu.cn; cgduan@clpm.ecnu.edu.cn

superlattice generates rich moiré band structures, which possess great potential for applications in actuators, mechanical sensors, transducers, and random-access memories[29–31]. Although the topological structure is depicted in twisted MoS_2 with large twist angles (>1.05°)[32], when the twist angles are decreased below the magic angle (<1.05°), more complex and diverse physical behaviors typically occur. However, identifying the continuous polar structures in the moiré system at microscopic twist angles remains a significant challenge.

In this study, we demonstrated a moiré ferroelectricity in twisted h-BN (t-BN) system. The relaxed atomic structure of t-BN is given in Fig. 1A, which are superimposed by BN layers with a small twist angle, θ. They interfere with each other, and create triangular moiré domains, due to atomic reconstruction. Based on systematically investigation, we identify that the moiré superlattice displays a complex polarization characteristic, and the polarization in configuration space is presented in Fig. 1B. By employing piezoelectric force microscopy (PFM), it is experimentally demonstrated that the sliding ferroelectric polarization in the centers of adjacent triangles is opposing due to a notable 180° phase difference. More interestingly, the in-plane (IP) polarization rotates clockwise or counterclockwise at the edges of adjacent triangles, and the edges are divided into two parts with opposite out-of-plane polarization, forming a more complex topological polarization network in the moiré system that is different from the traditional topologically non-trivial meron-antimeron structure (Fig. S1). In this case, this creates a toroidal or donut shaped configuration when viewed along the axis of rotation (Fig. 1C). The transition regions labeled by the black dash in Fig. 1B, like a Bloch-type domain walls in a moiré superlattice, is reported in the current work. The orientation of the polarization gradually rotates from down to up, then rotate back to down, and continuously from down to up (Fig. 1D). It should be noted that the electromechanically response at edge of triangle moiré patterns are much stronger than center regions, which is significantly different from conventional ferroelectrics, indicating a competition of underlying origins such as atomic reconstruction and charge redistributing etc. at the observed edges of moiré patterns.

Results

The t-BN samples are fabricated using the tear-and-stack method with both top and bottom layers of ~3 nm BN (Supplementary Fig. S2). The optical image is shown in Supplementary Fig. S3. The domain structures of the t-BN were characterized by PFM (Fig. 2A), in which the principle of lateral PFM is illustrated in Fig. 2B (principle of vertical PFM is given in Supplementary Fig. S4). When the tip encounters a region with different polarization vectors, it experiences a change in amplitude and phase of its vibration and torsion, which can be decomposed into two directions vertical ($dP_{\perp}$) and parallel ($dP_{\parallel}$) to the tip. The moirés in the region squared by the white dash in Fig. 2C is examined. It exhibits triangle moiré patterns with a length of 550–820 nm, and an edge width of ~100 nm (Fig. 2D, E). The lateral amplitude (L-Amp.) and phase contrast (L-Pha.) of each edge exhibit distinct behaviors when the scan angle between the tip and triangle's sides changes. The L-amp. response is the weakest when the cantilever (gray polygon) is parallel to the edge, and the strongest when the components are perpendicular to the cantilever (red and blue dash arrows). Since the polarization can point in any direction in three-dimensional space, information about triangle lengths and PFM response directions must be consulted in order to fully determine the polarization distribution in t-BN.

Taking the data in Fig. 2D, E as reference where the sample alignment angle is set as 0°, we conducted PFM imaging by rotating the sample counterclockwise in the increments of 30° for a set of given angles (Entire process is given in Supplementary Fig. S5). Figure 2D–I exhibit the typical L-Amp. and L-Pha. results with tip scanning along the three triangle's sides. The polar plot of edge L-amp. values can be found in Fig. 2J, and the profile values of L-amp. and L-pha. are given in Fig. 2K by extracting data from the red dash in Fig. 2D and the same

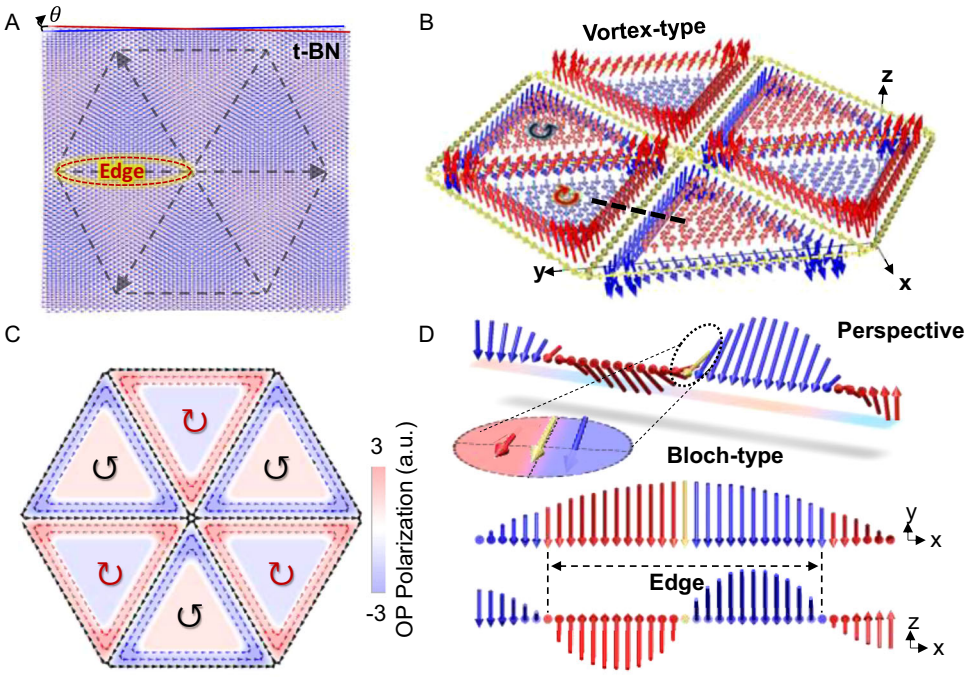

Fig. 1 | Schematic of complex polarization framework and unusual Bloch-type domain walls in t-BN. A Top view of the relaxed atomic structure of t-BN. **B** Perspective view of moiré structure. **C** Top view of IP polarization with clockwise and counterclockwise like merons and anti-merons. OOP polarization at the edge is displayed in the form of blue and red colors. The color bar represents the direction of OOP polarization. **D** Unusual Bloch-type domain walls with down-up-down-up polarization transitions.

https://doi.org/10.1038/s41467-025-58877-1

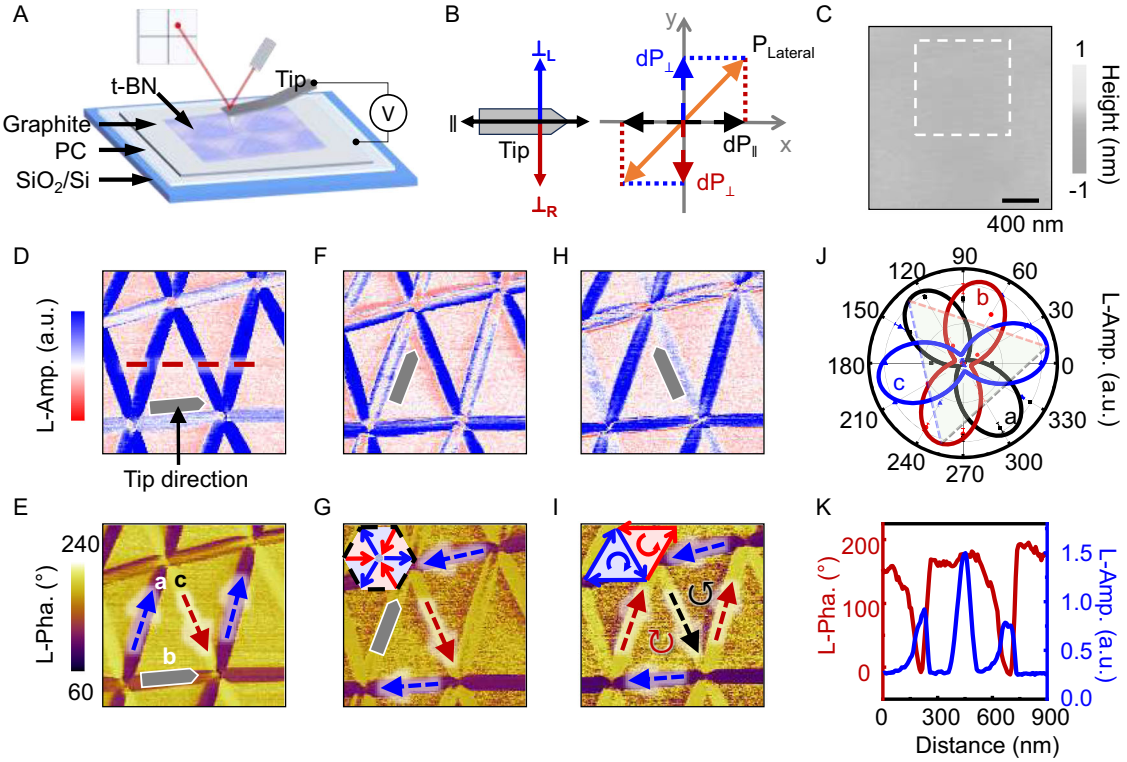

Fig. 2 | IP polarization in t-BN. A Schematic of PFM measurements. **B** Principle of lateral PFM. **C** Topography of t-BN. **D** L-Amp. and **E** L-Pha. of moiré domains at a tip-sample angle of 0°. **F** L-Amp. and **G** L-pha. signals measured at the same position with a tip-sample angle of 60°. **H** L-Amp. and **I** L-pha. responses obtained at a tip-sample angle of −60°.The gray tip represents the direction of the cantilever beam, and the red and blue dashed arrows in the phase image indicate the direction of IP polarization. **J** Polar plot of L-Amp. magnitude extracted from L-amp. images obtained at different tip-sample angles (from 0° to 360° with a step of 30°). **K** The profiles of L-Amp. and L-Pha. along the red dashed line in (**D**) and the same position in (**E**).

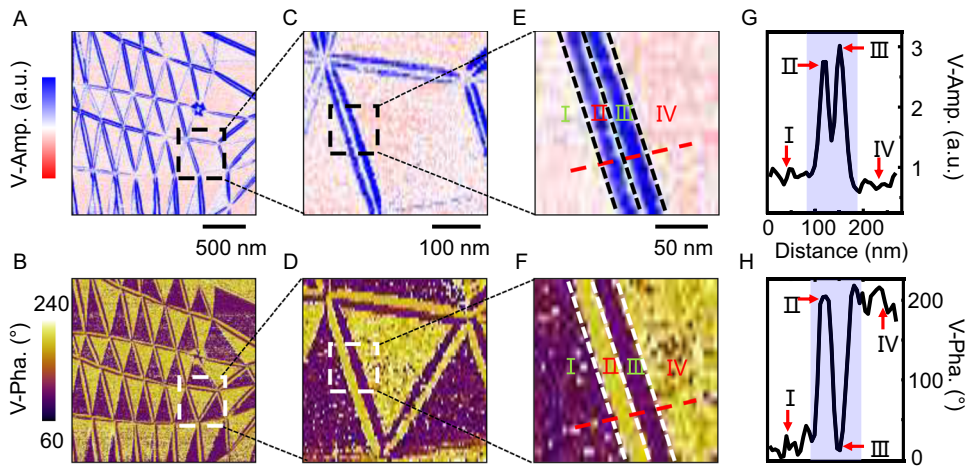

Fig. 3 | OOP two-lobe edge polarization with opposite direction in t-BN. **A** V-Amp. and **B** V-Pha. images at the same region in Fig. 2. **C** The enlarged V-Amp. and **D** V-Pha. at the regions within the black dashed boxes in (**A**) and (**B**). **E** Zoomed V-Amp. and **F** V-Pha. at the edge labeled by black dash squares in (**C**) and (**D**). **G** The profiles of V-Amp. and **H** V-Pha. extracted along the red dashes highlighted in (**E**) and (**F**).

position in Fig. 2E (Larger range is given in Supplementary Figs. S7-8). Figure 2K shows strong L-amp. responses at edge (blue curve) and ~180° phase difference between adjacent edges (red curve), indicating significant edge effects. The results that IP polarization is detectable close to the edge of triangular moiré patterns, demonstrating IP polarization is aligned to the sides of triangular moiré patterns. Moreover, IP polarizations appear to be connected head-to-tail along the edges and rotate along the center axis of each triangle, suggesting a clockwise and counterclockwise IP polarizations. In a word, it exhibits a topological polarization network like merons and antimerons (Supplementary Fig. S6) in t-BN superlattice. The schematic of domain and domain wall in x-y plane is given in Fig. 1C, D, which is highly identical to the L-PFM results shown in Fig. 2.

Different from IP topological domains in t-BN, out-of-plane (OOP) polarizations for the same edges are surprisingly split into two parts, as shown in Fig. 3C–F. The domains are also checked by rotating the sample 90° to exclude the IP vectors and topography crosstalk (Supplementary Fig. S9). However, the OOP phase difference between

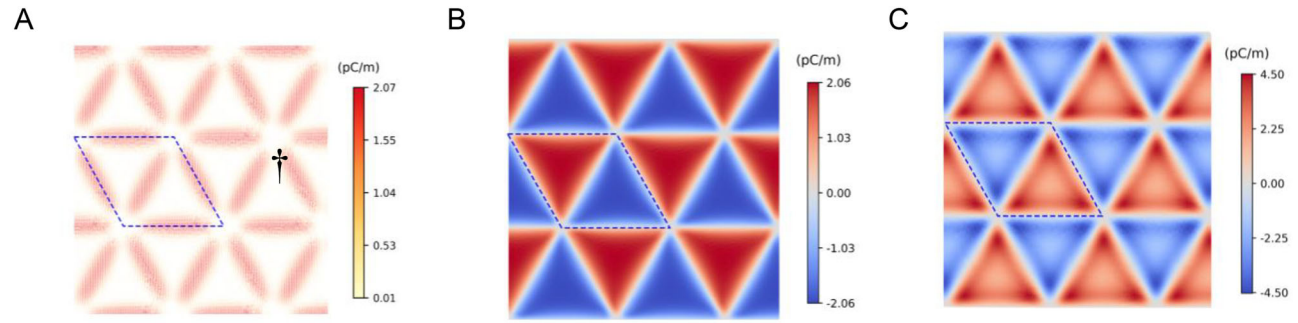

Fig. 4 | Polarization pattern in relaxed bilayer twisted h-BN. A IP polarization distribution in relaxed h-BN with twist angle of 0.99°. The length and color intensity of the arrows represent the magnitude of polarization. **B** OOP ferroelectricity distribution, as predicted by the DP-JAX model, in relaxed h-BN with a twist angle of 0.99°. **C** OOP polarization induced by piezoelectric effects.

adjacent patterns with AB and BA stacking is much smaller than 180°, consisting with previous works[23], which is contrast with the proposed opposite polarization in AB and BA stacking. To suppress the electrostatic influence, we employed PFM technique (Quadrature Phase Differential Interferometry, QPDI) measurement, and Fig. 3A, B show the OOP PFM results. The region near the edge within the black and white labeled in Fig. 3A, B is zoomed in Fig. 3C–F, and values along the red dashes labeled in Fig. 3E, F are extracted in Fig. 3J, H. The distinct amplitude and phase contrast in the adjacent centers of triangular moiré pattern is, namely, regions I and IV. The phase contrast between them is ~180°, and the difference of amplitude response (Fig. 3A) is obvious, suggesting opposite OOP polarization direction. Meanwhile, OOP PFM responses at edge, regions II and III, are also distinguished, which is very consistent with IP signals. The amplitude intensity of edge is higher than the centers, while the phase contrast between II and III is ~180°, indicating another opposite OOP polarization direction.

Notably, the adjacent center and edge also present opposite polarization direction (region I and II). The polarization vectors near the edge experience OOP down-up-down-up switching and keep the IP component direction the same (unusual Bloch-type). The schematic of OOP edge is given in Fig. 1D (z-x plane and perspective view), which is in accordance with both V- and L-PFM. By evaluating the L- and V-PFM results (Figs. 2 and 3), diagram can be built in 3D space, as shown in Fig. 1B. The polarization topology in t-BN possess a complex network like merons and anti-merons assembled in the edge of triangle moirés, and unusual Bloch-type domain walls at the edges (Fig. 1D). Distinguish from strong center polarization in conventional ferroelectric materials, it should be noted that polarization in t-BN system is more prominent in edge of moiré patterns. In addition to t-BN, similar phenomena including IP and OOP were also observed in twisted WSe_2 (Supplementary Figs. S10, 11). Moreover, the complex polar topological structure is consistent in moiré patterns with different twist angles (twist angle≪1°) (Supplementary Figs. S12–15), indicating that such configuration is suitable for different moiré systems.

To understand the moiré ferroelectricity in t-BN, a deep potential model using machine learning methods combining with first-principle calculations[24] is adopted to handle the twisted systems which generally contain tens of thousands of atoms (details are given in Methods and Supplementary Fig. S16, 17). We get the relaxed atomic distribution for h-BN moiré structure at a twist angle of 0.99° (Fig. 1A), consisting of triangular domains of dominant AB or BA stackings, and saddle point (SP) at the boundary of adjacent triangles, which is corresponding to middle of moiré pattern edge[33]. In contrast with AB/BA stackings, SP has the highest IP polarization and zero OOP polarization, which is identical with our experimental results as shown in Figs. 2 and 3. Then, a DP-JAX model, mapping the dipole moments of bilayer h-BN with the local atomic structure, is trained to predict the local polarization distribution in the relaxed h-BN moiré structure. Local polarization in adjacent triangles before relaxation is given in Supplementary Fig. S18, exhibiting vortex distributions in reverse directions[27]. IP polarization under relaxation effects, as presented in Fig. 4A, is mainly concentrated along the edges of the triangles, which is consistent to our L-PFM results (Fig. 2). However, OOP polarization predicted by the model is merely exist in triangle domains, no edge polarization around SP regions is observed (Fig. 4B), contradictory to V-PFM measurements (Fig. 3).

Note that although DP-JAX model is effective to capture the contribution from short-range sliding ferroelectricity[10], it ignores long-range flexoelectric and piezoelectric effects in the SP regions of moiré systems[34]. These might play an important role in global polarization distribution, and thus explaining the unique edge polarization. According to the OOP displacement field, flexoelectric effects is ruled out as a key factor in this case since it would induce polarization in the same direction between adjacent triangle domains, and is anticipated to be countered by the opposing reconstruction between top and bottom layers. This is contradicting to our experimental findings that edge possesses two opposite OOP polarizations (Fig. 3). Therefore, model analysis of piezoelectric effect in the dipole distribution within this system is carried out. For each layer, atomic reconstruction causes an IP strain field (Supplementary Fig. S19), resulting in the distribution of IP polarization due to piezoelectric effect (Supplementary Fig. S20). However, two adjacent layers have opposite atomic displacement patterns (Supplementary Fig. S21), leading to compensated IP polarization, and thus leaving no effect on the global IP polarization.

Nevertheless, IP polarization induced by piezoelectric effect can induce IP charge distribution (Supplementary Fig. S22). The opposite IP polarization in each layer can lead to reversed piezoelectric charge distribution between them[35]. Meanwhile, the charge pattern induced by piezoelectric effects is found to be angle-dependent. The induced charges accumulate in the center (triangular domains) when the twist angle is large (Supplementary Fig. S22E, F), while distribute along the edge if the twist angle is small (Supplementary Fig. S22A–D)[28]. Interestingly, the piezoelectric charges with opposite signs and uniform IP projection in adjacent layers can create a vertical potential drop, and thus bringing out OOP polarization[36]. Moreover, the introduced polarization direction at the two-lobe edge is opposite (one lobe is polarized upward while the other one with downward polarization), and the polarization intensity decrease from the edges to the centers (Fig. 4C), which aligns well with our experimental observations (Fig. 3). In the experiment, the tested moiré pattern twist angles are all less than 1°.

The moiré structure constituted by the unique edges induced by piezoelectric and sliding effects (Figs. 2, 3) is inherently stable due to the nontrivial topology. Although the fact that the generation and manipulation of vortex (AB/BA)-antivortex (AA) pairs can be facilitated

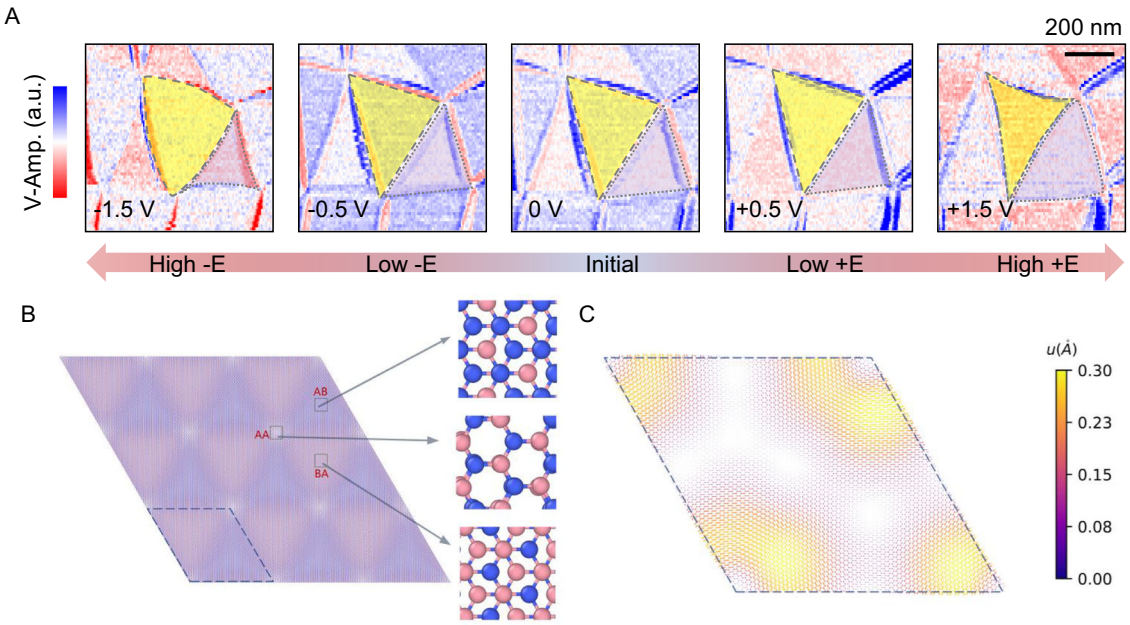

Fig. 5 | Moiré pattern under an applied electric field. A V-Amp. images under different biases. **B** Expansion (composed of BA stacking) and contraction (composed of AB stacking) of ferroelectric domains under an electric field of 0.5 V/Å, while the area of AA stacking does not show significant change. **C** In-plane atomic displacement of upper layer after structural reconstruction under the effect of electric field.

through localized electric fields, the robustness of the vortex and antivortex cores usually exhibit resistance to movement, providing a robust framework capable of withstanding perturbations. As depicted in Fig. 5A, the moiré topological pattern persists under a minor OOP bias, preserving the triangular architecture unchanged. When a more substantial bias of ±1.5 V is applied, edge dynamics are initiated, causing AB, BA, and edge regions to adjust and reach energy equilibrium, with energy-unfavorable triangles contracting while the adjacent ones expand. Notably, despite the deformation of edges induced by an external electric field, the cores of antivortices and vortices remain stable, and the AA regions remain almost unchanged. These findings are in accordance with our theoretical model, where the core of the vortex/antivortex polarization pattern remains in the same stacking modes under the effect of electric field (Fig. 5B). Additionally, the IP atomic displacement after lattice reconstruction also shows minimal variation upon the application of electric field (Fig. 5C), indicating the piezoelectricity-induced edge polarization is robust to such external influences.

In conclusion, we propose a robust edge topology that features IP like meron-antimeron polarization. The edge consists of two splitting regions with opposite OOP polarizations and a complete IP topological structure. The adjacent triangular moiré patterns in the center only possess opposite OOP polarizations. Through our theoretical investigation, we identify that the combined sliding ferroelectricity and piezoelectric effects are the physical origin of the complex polarization characteristics in twisted BN. The stability of vortex-antivortex structures with unique edges is significantly influenced by their topological characteristics, which is essential for the development of devices that rely on these topological features, ensuring remarkable reliability and durability even under varying external perturbations. Our discovery provides new insights into unconventional interfacial ferroelectrics in moiré systems, opening up new opportunities for fundamental research and applications in electronics and data storage.

Methods

Sample fabrication

Sample fabrication and hexagonal boron nitride (h-BN) are exfoliated and identified through optical microscopy. The thickness of these thin layers is then determined using an atomic force microscope (AFM). A polycarbonate (PC) film on PDMS is used to extract graphene from the SiO_2 substrate to serve as the bottom gro cation. The twisted boron nitride (t-BN) is prepared using the tear-and-rotate technique (Supplementary Fig. S1). On a SiO_2 (300 nm)/Si substrate, grapheneund electrode. Meanwhile, the AFM probe is utilized to cut the BN layer into two pieces, BN1 and BN2. The sample stage is heated to 90 °C, and with careful manipulation using the pre-constructed PDMS/PC/graphene setup, BN1 is extracted and moved parallel to the sample stage to cover BN2. The PC film is peeled off from PDMS and transferred onto the SiO_2/Si substrate, then heated to 100 °C to enhance adhesion between the substrate and the film. Thick graphite extracted using PDMS is placed as an electrode on top of the underlying graphene. The optical image of the obtained t-BN is shown in Supplementary Fig. S2.

Scanning Probe Microscopy*(SPM) characterization*

A commercial SPM (Cypher S, Asylum Research) including Piezoelectric force microscopy (PFM) is employed in this investigation. All experiments were conducted under ambient atmospheric conditions at room temperature. Conductive probes (NSC18, MicroMasch) with platinum (Pt) coating were used. The vertical PFM (V-PFM) contact resonance frequency was set to approximately 340 kHz, while the lateral PFM (L-PFM) contact resonance frequency was about 620 kHz. An alternating current (AC) voltage of 1.5 V was applied throughout the PFM measurements. The PFM phase originates from polarization reversal, which can be verified by QPDI (Quadrature Phase Differential Interference) -PFM measurements (a 180° PFM phase difference exists in oppositely polarized regions). QPDI allows for the measurement of pure vertical probe displacement, unaffected by cantilever bending and avoiding electrostatic artifacts. The QPDI-PFM measurements were conducted using a commercial Vero AFM (Asylum Research, Oxford Instruments), as shown in Fig. 3, during the testing process, an alternating current of 1 V was applied.

Machine learning

Energy model. Deep neural network-based potential model is used to describe atomic interactions in moiré systems, effectively resolving the challenge of balancing accuracy and efficiency in large-scale

atomistic relaxations. Using the training datasets from first-principle calculations, we employ the deep potential (DP) method[37,38] to train a deep neural network potential for h-BN bilayer. In other words, the DP model is to learn the connection between atomic distribution and the interatomic potential energy and force field, thus selecting appropriate configurations for the training dataset is vital for an accurate model[39,40]. Moiré bilayer system contains all characteristic structures of various stacking modes, including the intermediate states of interlayer sliding, IP distortion as well as interlayer warping. Manual construction of all these configurations is very laborious. Therefore, we explored configurations by running AIMD simulations on VASP. The initial dataset contains AB, AA, AA′, SP along with seven other bilayer stacking modes which have all been optimized by DFT calculations and expand to 4*4 supercells with 64 atoms. 2000-step AIMD simulations using the canonical ensemble were performed at 300 K for each initial stacking configurations (such as AB). It is worth mentioning that the MD trajectories have covered all stacking configurations, which is strong evidence of the comprehensive coverage of our datasets. After AIMD simulations, we got 22000(11*2000) configurations for the datasets. Next, we trained the DP model by the DeePMD-kit code[37] in which the total potential energy of a configuration is assumed to be a sum of atomic energies mapped from a descriptor through an embedding network. 4400 configurations of the training data are used for validations. The sizes of the embedding and fitting networks are (25, 50, 100) and (240, 240, 240), respectively, and the cutoff radius for each atom is 6.0 Å. The DP model was trained with 1,760,000 steps with a batch size of 1, thereby minimizing the loss function that including energy and atomic force contributions. To evaluate the performance of the DP model, we compared the energies and atomic forces for all configurations in the validation datasets using both DFT and the DP model (Supplementary Fig. S11A–C). The DP model is used to relax the superlattice within the LAMMPS package[41].

Energy model with electric field

Based on the method training the intrinsic BN energy model, we trained an energy model under an applied electric field of 0.5 V/Å. First-principles datasets of the structure and energy were obtained by running AIMD simulations in VASP, with an 0.5 V/Å electric field applied along the out-of-plane axis. The DP model was trained over 1,200,000 steps. Same relaxation method was then used to get the moire structure under the influence of electric field.

DFT calculations

We use the Vienna ab initio simulation package (VASP)[42] with projector augmented wave method[43,44] and the generalized gradient approximation (GGA) with Perdew-Burke-Ernzerh (PBE) of exchange-correlation functional[45]. A plane-wave cutoff energy of 500 eV in the structural relaxation calculations was adopted. Van der Waals corrections are employed using DFT-D2 method of Grimme[46]. A large distance of c>15Å along the out-of-plane direction is applied to eliminate interlayer interactions. A $2\times2\times1$ k-point mesh is sufficient to converge the energy and atomic force for the $4\times4\times1$ supercell with 64 atoms for AIMD calculation, preparing datasets for model training. The optimized lattice constant of AB stacked bilayer h-BN is a = b = 2.509Å with interlayer distance 3.08Å. The Berry phase method results in a calculated perpendicular polarization of the h-BN's AB domain of $P_z = 2.06\times10^{-12}$C/m, consistent with previous theoretical work[10]. To validate the accuracy of our energy model, we also calculate phonon properties of a relaxed h-BN moiré structure with a large twist angle using density-functional perturbation theory[47] (Supplementary Fig. S11E, F)).

Polarization model

Apart from scalar properties like force and energy, deep potential can also be used to fit high-dimensional physical quantities like local dipole moments[38]. For a better understanding of the topological polarization in a real place of a relaxed moiré system, we use DeepMD-JAX package to train a model fitting the local dipole distributions of the h-BN bilayer moiré structure. Compared with the DP model with tensor flow backbend, DP-JAX model, implementing the new scheme with JAX, performs better on the training accuracy as well as training speed[34]. The total polarization of a crystal μ can be conveniently expressed as the sum of the dipole moments of ions and of the wannier centres(w_k), the latter can be calculated by the maximally localized wannier functions(MLWFs)[48,49]. In a spin-saturated system, the MLWFs describe electron pairs, thereby assigning charges of $2e^-$ to wannier centres, accordingly, the microscopic polarization is:

$$\boldsymbol{\mu} = e\sum_i Z_i \mathbf{r_i} - 2e\sum_k \mathbf{w_k} \tag{1}$$

where e is the unit electronic charge, Z_i are atomic numbers, $\mathbf{r_i}$ are the position vectors of the nuclei. The Wannier centers are obtained from a unitary transformation that minimizes the spatial spread in the occupied orbital subspace. We use a valence-only pseudopotential approach, where the nuclear charges eZ_i represent the ions consisting of the nuclei and the frozen core electrons, while the Wannier centers correspond to the valence electrons. Specializing to h-BN, which contains boron ($\mathbf{r_{B_i}}$) and nitride ($\mathbf{r_{N_i}}$) ions, wannier centers are only associated with N, the most electronegative atoms during molecular evolution, the polarization vector is:

$$\boldsymbol{\mu} = 3e\sum_i \mathbf{r_{B_i}} + 5e\sum_i \mathbf{r_{N_i}} - 2e\sum_k \mathbf{w_k} \tag{2}$$

Based on this principle, we calculated the polarization of the relaxed bilayer h-BN unit cell with different stackings. The results closely matched the polarization calculated using the Berry phase method, as shown in Supplementary Fig. S6a, demonstrating the feasibility of using Wannier centers to compute local polarization. Using the polarization dataset obtained through the Wannier center approach, we trained the DP-JAX model capable of predicting dipole distribution in bilayer h-BN superlattices. The dipole distribution for unrelaxed twisted bilayer h-BN is consistent with previous work. We have benchmarked our model by comparing the polarization results of the DP model with DFT calculations for all configurations in the validation dataset (Supplementary Fig. S12A–C). Besides, the polarization predicted by our model for the relaxed bilayer h-BN unit cell with different stackings, as shown in Supplementary Fig. S12D, also aligns well with the results obtained using the Berry phase method. Consequently, it is reasonable to expect that our model will perform well on relaxed moiré systems as well.

The calculations of the polarization induced by piezoelectric effects

Since monolayer h-BN has the symmetry of C3, the only independent non-zero piezoelectric coefficient is $\tilde{e}_{11} \equiv \tilde{e}_{111}$. Other non-zero coefficients are related to $\tilde{e}_{11}$ by[50]

$$\tilde{e}_{122} = \tilde{e}_{212} = -\tilde{e}_{11}. \tag{3}$$

Using the berry phase method in VASP[51], $\tilde{e}_{11}$ can be calculated from the change of IP polarization with respect to the strain. Density functional perturbation theory can also be used to obtain $\tilde{e}_{11}$[52,53], the result is consistent with the berry phase method as well as previous calculations[50]. The piezoelectric polarizations in the moiré superlattice

can be expressed as the function of strain tensor u,

$$\mathbf{P} = \widetilde{e}_{11}\left(u_{xx} - u_{yy}, -2u_{xy}\right), \tag{4}$$

where u_{xx}, u_{yy}, u_{xy} arise from IP atomic displacement under the relaxation effects. Accordingly, the piezoelectric charge density is the divergence of the piezoelectric polarization,

$$\rho_{piezo} = -\nabla \cdot \mathbf{P} = -\widetilde{e}_{11}\left[\partial_x\left(u_{xx} - u_{yy}\right) - 2\partial_y u_{xy}\right]. \tag{5}$$

Due to the equal magnitude and opposite sign of the charge densities at the same IP position for the two layers, vertical polarization is created by the interlayer potential drop,

$$\mathbf{P}_{\perp} = d * \rho_{piezo} = -d\widetilde{e}_{11}\left[\partial_x\left(u_{xx} - u_{yy}\right) - 2\partial_y u_{xy}\right], \tag{6}$$

where d is the interlayer distance at the local unit cell in the moiré structure. This is the polarization induced by piezoelectric effects.

Data availability

The authors declare that the data supporting the findings of this study are available within the paper and its Supplementary Information files. Additional data are available from the corresponding author upon reasonable request.

References

1. Han, L. et al. High-density switchable skyrmion-like polar nanodomains integrated on silicon. *Nature* **603**, 63–67 (2022).
2. Cao, Y. et al. Unconventional superconductivity in magic-angle graphene superlattices. *Nature* **556**, 43–50 (2018).
3. Cao, Y. et al. Correlated insulator behaviour at half-filling in magic-angle graphene superlattices. *Nature* **556**, 80–84 (2018).
4. Serlin, M. et al. Intrinsic quantized anomalous Hall effect in a moiré heterostructure. *Science* **367**, 900–903 (2020).
5. Zubko, P. et al. Negative capacitance in multidomain ferroelectric superlattices. *Nature* **534**, 524–528 (2016).
6. Can, O. et al. High-temperature topological superconductivity in twisted double-layer copper oxides. *Nat. Phys.* **17**, 519–524 (2021).
7. Song, Z. et al. All Magic Angles in Twisted Bilayer Graphene are Topological. *Phys. Rev. Lett.* **123**, 036401 (2019).
8. Lian, B., Liu, Z., Zhang, Y. & Wang, J. Flat Chern Band from Twisted Bilayer MnBi2Te4. *Phys. Rev. Lett.* **124**, 126402 (2020).
9. Yoo, H. et al. Atomic and electronic reconstruction at the van der Waals interface in twisted bilayer graphene. *Nat. Mater.* **18**, 448–453 (2019).
10. Li, L. & Wu, M. Binary Compound Bilayer and Multilayer with Vertical Polarizations: Two-Dimensional Ferroelectrics, Multiferroics, and Nanogenerators. *ACS Nano* **11**, 6382–6388 (2017).
11. Fei, Z. et al. Ferroelectric switching of a two-dimensional metal. *Nature* **560**, 336–339 (2018).
12. Woods, C. R. et al. Charge-polarized interfacial superlattices in marginally twisted hexagonal boron nitride. *Nat. Commun.* **12**, 347 (2021).
13. Vizner Stern, M. et al. Interfacial ferroelectricity by van der Waals sliding. *Science* **372**, 1462–1466 (2021).
14. Yasuda, K., Wang, X., Watanabe, K., Taniguchi, T. & Jarillo-Herrero, P. Stacking-engineered ferroelectricity in bilayer boron nitride. *Science* **372**, 1458–1462 (2021).
15. Kim, D. S. et al. Electrostatic moiré potential from twisted hexagonal boron nitride layers. *Nat. Mater.* **23**, 65–70 (2023).
16. Guan, Z. et al. Mechanical force-induced interlayer sliding in interfacial ferroelectrics. *Nat. Commun.* **16**, 986 (2025).
17. Tang, H. et al. On-chip multi-degree-of-freedom control of two-dimensional materials. *Nature* **632**, 1038–1044 (2024).
18. Deb, S. et al. Cumulative polarization in conductive interfacial ferroelectrics. *Nature* **612**, 465–469 (2022).
19. Ko, K. et al. Operando electron microscopy investigation of polar domain dynamics in twisted van der Waals homobilayers. *Nat. Mater.* **22**, 992–998 (2023).
20. Li, Y. et al. Topological Polar Networks in Twisted Rhombohedral-Stacked Bilayer WSe_2 Moiré Superlattices. *Nano Lett.* **24**, 13349–13355 (2024).
21. Niu, R. et al. Giant ferroelectric polarization in a bilayer graphene heterostructure. *Nat. Commun.* **13**, 6241 (2022).
22. Wang, X. et al. Interfacial ferroelectricity in rhombohedral-stacked bilayer transition metal dichalcogenides. *Nat. Nanotechnol.* **17**, 367–371 (2022).
23. McGilly, L. J. et al. Visualization of moiré superlattices. *Nat. Nanotechnol.* **15**, 580–584 (2020).
24. Lv, M. et al. Spatially Resolved Polarization Manipulation of Ferroelectricity in Twisted hBN. *Adv. Mater.* **34**, 2203990 (2022).
25. Enaldiev, V. V., Ferreira, F., Magorrian, S. J. & Fal'ko, V. I. Piezoelectric networks and ferroelectric domains in twistronic superlattices in WS2 /MoS2 and WSe/MoSe2 bilayers. *2D Mater.* **8**, 025030 (2021).
26. Zhu, R. et al. Atomic-Scale Tracking Topological Phase Transition Dynamics of Polar Vortex-Antivortex Pairs. *Adv. Mater.* **36**, 2312072 (2024).
27. Bennett, D., Chaudhary, G., Slager, R.-J., Bousquet, E. & Ghosez, P. Polar meron-antimeron networks in strained and twisted bilayers. *Nat. Commun.* **14**, 1629 (2023).
28. Zhang, X.-W. et al. Polarization-driven band topology evolution in twisted MoTe2 and WSe2. *Nat. Commun.* **15**, 4223 (2024).
29. Scott, J. F. Applications of Modern Ferroelectrics. *Science* **315**, 954–959 (2007).
30. Wang, Y. J., Tang, Y. L., Zhu, Y. L. & Ma, X. L. Entangled polarizations in ferroelectrics: A focused review of polar topologies. *Acta Mater.* **243**, 118485 (2023).
31. Lau, C. N., Bockrath, M. W., Mak, K. F. & Zhang, F. Reproducibility in the fabrication and physics of moiré materials. *Nature* **602**, 41–50 (2022).
32. Tsang, C. S. et al. Polar and quasicrystal vortex observed in twisted-bilayer molybdenum disulfide. *Science* **386**, 198–205 (2024).
33. He, R. et al. Ultrafast switching dynamics of the ferroelectric order in stacking-engineered ferroelectrics. *Acta Mater.* **262**, 119416 (2024).
34. Gao, R., Li, Y. & Car, R. Enhanced deep potential model for fast and accurate molecular dynamics: application to the hydrated electron. *Phys. Chem. Chem. Phys.* **26**, 23080–23088 (2024).
35. Enaldiev, V. V., Zólyomi, V., Yelgel, C., Magorrian, S. J. & Fal'ko, V. I. Stacking Domains and Dislocation Networks in Marginally Twisted Bilayers of Transition Metal Dichalcogenides. *Phys. Rev. Lett.* **124**, 206101 (2020).
36. Magorrian, S. J. et al. Multifaceted moiré superlattice physics in twisted WSe 2 bilayers. *Phys. Rev. B* **104**, 125440 (2021).
37. Wang, H., Zhang, L., Han, J. & E, W. DeePMD-kit: A deep learning package for many-body potential energy representation and molecular dynamics. *Comput. Phys. Commun.* **228**, 178–184 (2018).
38. Zeng, J. et al. DeePMD-kit v2: A software package for deep potential models. *J. Chem. Phys.* **159**, 054801 (2023).
39. Zhang, L., Han, J., Wang, H., Car, R. & E, W. Deep Potential Molecular Dynamics: A Scalable Model with the Accuracy of Quantum Mechanics. *Phys. Rev. Lett.* **120**, 143001 (2018).
40. Zhang, L. et al. End-to-end symmetry preserving inter-atomic potential energy model for finite and extended systems. In: *Proceedings of the 32nd International Conference on Neural Information Processing Systems* 4441–4451 (Curran Associates Inc., 2018).

41. Thompson, A. P. et al. LAMMPS - a flexible simulation tool for particle-based materials modeling at the atomic, meso, and continuum scales. *Comput. Phys. Commun.* **271**, 108171 (2022).
42. Kresse, G. & Furthmüller, J. Efficiency of ab-initio total energy calculations for metals and semiconductors using a plane-wave basis set. *Computational Mater. Sci.* **6**, 15–50 (1996).
43. Blöchl, P. E. Projector augmented-wave method. *Phys. Rev. B* **50**, 17953–17979 (1994).
44. Kresse, G. & Joubert, D. From ultrasoft pseudopotentials to the projector augmented-wave method. *Phys. Rev. B* **59**, 1758–1775 (1999).
45. Perdew, J. P., Burke, K. & Ernzerhof, M. Generalized Gradient Approximation Made Simple. *Phys. Rev. Lett.* **77**, 3865–3868 (1996).
46. Grimme, S. Semiempirical GGA-type density functional constructed with a long-range dispersion correction. *J. Computational Chem.* **27**, 1787–1799 (2006).
47. Gonze, X. & Lee, C. Dynamical matrices, Born effective charges, dielectric permittivity tensors, and interatomic force constants from density-functional perturbation theory. *Phys. Rev. B* **55**, 10355–10368 (1997).
48. Marzari, N. & Vanderbilt, D. Maximally localized generalized Wannier functions for composite energy bands. *Phys. Rev. B* **56**, 12847–12865 (1997).
49. Marzari, N., Mostofi, A. A., Yates, J. R., Souza, I. & Vanderbilt, D. Maximally localized Wannier functions: Theory and applications. *Rev. Mod. Phys.* **84**, 1419–1475 (2012).
50. Duerloo, K.-A. N., Ong, M. T. & Reed, E. J. Intrinsic Piezoelectricity in Two-Dimensional Materials. *J. Phys. Chem. Lett.* **3**, 2871–2876 (2012).
51. Spaldin, N. A. A beginner's guide to the modern theory of polarization. *J. Solid State Chem.* **195**, 2–10 (2012).
52. Gajdoš, M., Hummer, K., Kresse, G., Furthmüller, J. & Bechstedt, F. Linear optical properties in the projector-augmented wave methodology. *Phys. Rev. B* **73**, 045112 (2006).
53. Baroni, S. & Resta, R. Ab initio calculation of the macroscopic dielectric constant in silicon. *Phys. Rev. B* **33**, 7017–7021 (1986).

Acknowledgements

National Key Research and Development Program of China grant 2024YFA1409700 and 2022YFA1402902; National Natural Science Foundation of China grant 12474084, 12204171, 12134003, 12374145, 12304218; Chenguang Program of Shanghai Education Development Foundation and Shanghai Municipal Education Commission; Shanghai Pujiang Program grant 23PJ1402200; ECNU (East China Normal University) Multifunctional Platform for Innovation (006); Fundamental Research Funds for the Central Universities.

Author contributions

W.C.F., Z.G. and L.Q.W. performed the PFM experiments supervised by N.Z. and P.H.X.; H.W.X., C.S.Y., J.D.Z. performed the DFT calculations supervised by W.Y.T. and C.G.D.; M.T. and N.W. grew the h-BN crystals; Z.G., L.Q.W., W.C.F., W.Y.T., B.B.C., P.X.H, C.G.D., and N.Z. discussed the results. discussed the results and contributed to the writing of the manuscript.

Competing interests

The authors declare no competing interests.

Additional information

Supplementary information The online version contains supplementary material available at https://doi.org/10.1038/s41467-025-58877-1.

Correspondence and requests for materials should be addressed to Ping-Hua Xiang, Ni Zhong or Chun-Gang Duan.

Peer review information *Nature Communications* thanks the anonymous, reviewer(s) for their contribution to the peer review of this work. A peer review file is available.